Modular Redox Switching of Dinuclear Organometallic Molecular Junctions

Yuya Tanaka,*[1,2†] Naoki Morozumi,[2†] Tatsuhiko Ohto,[3,4] Satoshi Kaneko,[5] Yasuhisa Naitoh,[6] Hirokazu Tada,[3] Shintaro Fujii,[5] Tomoaki Nishino,[5] Munetaka Akita*[1,2]

[1]*Laboratory for Chemistry and Life Science, Institute of Innovative Research, Tokyo Institute of Technology, 4259 Nagatsuta, Midori-ku, 226-8503, Yokohama, Japan.*

[2] *Department of Chemical Science and Engineering, School of Materials and Chemical Technology, Tokyo Institute of Technology, 4259 Nagatsuta, Midori-ku, 226-8503, Yokohama, Japan.*

[3] *Graduate School of Engineering Science, Osaka University*

1-3 Machikaneyama, Toyonaka, Osaka 560-8531, Japan

[4] *Center for Quantum Information and Quantum Biology, Institute for Open and Transdisciplinary Research Initiatives, Osaka University, 1-3 Machikaneyama, Toyonaka, Osaka 560-8531, Japan*

[5] *Department of Chemistry, School of Science, Tokyo Institute of Technology, 2-12-1 Ookayama, Meguro-ku, 152-8551, Tokyo, Japan.*

[6] *National Institute of Advanced Industrial Science and Technology, Tsukuba, Ibaraki 305-8565, Japan*

KEYWORDS. single-molecule conductance, redox-responsive molecular switch, mixed-valence species, break junction, ruthenium acetylides.

ABSTRACT: A molecular switch is one of the essential functional components of molecular electronics. Herein, we report the development of new molecular switches based on electron-rich diruthenium complexes with (2,5-di-R-substituted 1,4-diethynylbenzene)diyl linkers. The dinuclear molecular switches, {μ–*p*–C≡C–(2,5-R_2-C_6H_2)–C≡C}{Ru(dppe)$_2$(C≡C–C_6H_4-*p*-SMe)}$_2$ **1^R**, with various substituents (R = OMe, H, or CF_3) on the bridging phenylene rings exhibited two successive reversible 1e-oxidation waves, evidencing the stability of 1e-oxidized mixed-valence species. The solid-state structure of [**1^H**]$^+$ enabled its charge-localized Robin–Day class II nature, while [**1^{OMe}**]$^+$ exhibited the fully charge-delocalized class III character. These characters were further confirmed by the spectroscopic data obtained in solution. Single-molecule conductance measurements by the scanning tunneling microscope break-junction (STM-BJ) method revealed the significant dependence of the conductance on R. The conductance of **1^{OMe}** was over 100 times higher than those of **1^H** and **1^{CF3}**, whereas the substituent effect of the monocationic complexes was within a fold-change of 2. Consequently, the ON/OFF ratios (the ratios of the conductances of the cationic species [**1^R**]$^+$ to those of the neutral species, **1^R**) were critically dependent on R (as large as 191 for R = CF_3) and even reversed (0.4 for R = OMe). Furthermore, the neutral and monocationic complexes, **1^H** and [**1^H**]$^+$, fabricated into the nanogap devices exhibited the *in-situ* ON/OFF switching behavior. The present study demonstrates not only rare examples of mixed-valence complexes that are subjected to the break-junction measurements, but also the first examples of molecular switches, the ON/OFF ratios of which are controlled by tuning the organic linker parts.

INTRODUCTION

A molecular switch, which controls a specific function reversibly when acted upon by an external stimulus, is an essential component of molecule-based electronics. To date, many studies have been conducted on various molecular switches incorporated into metal–molecule–metal junctions, which are responsive to mechanical,[1–3] acid–base,[4,5] photoirradiation,[6–8] and redox stimuli.[9,10] Redox stimulus is superior to other stimulus types because the trigger can be easily fabricated by the installation of a third electrode into nanodevices, in addition to the drain and source electrodes.[11] Some redox-triggered organic molecular switches have been reported. For example, Campos et al. investigated an aromatic bifluorenylidene-based redox switch, which was converted into the antiaromatic dicationic state upon 2e-oxidation (Figure 1a).[10] A high ON/OFF ratio (the ratio of the conductances in the ON and OFF states) with a factor of 70 was reported. Further, multiple switching behavior was reported for the naphthalenediimide derivative (Figure 1b).[9] Stepwise 1e-reduction led to mono- and di-anionic states, and the conductance in the monoanionic state was 10 times higher than that in the neutral state. For the redox switch, however, two key limitations require solutions: (1) the instability of the oxidized or reduced radical species formed upon application of redox stimuli, and (2) the lack of a rational molecular design for modulating/controlling the ON/OFF ratio without interfering with the original switching function.[12]

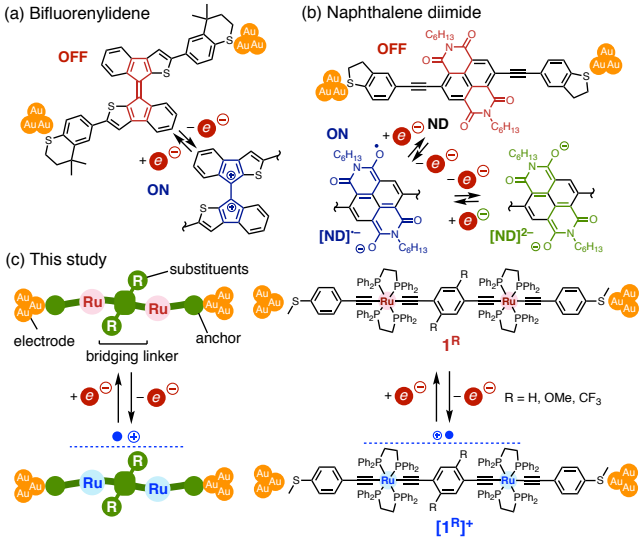

Figure 1. Organic molecular switches based on (a) bifluorenylidene and (b) naphthalene diimide. (c) Concept of the present redox-responsive dinuclear molecular switches, **1**^{R}–**[1**^{R}**]**$^{+}$ (R = OMe, H, or CF_3).

Among mixed-valence (MV) species, dinuclear systems composed of two metal centers with different oxidation states (M/M$^{\bullet+}$) are attracting significant interest. In many cases, these metal centers are bridged by an organic ligand (BL),[13] i.e., M–BL–M$^{\bullet+}$, and are considered to be excellent model systems for examining the Marcus-type charge-transfer phenomena in solutions. A charge carrier (electron or hole) can be transferred from one metal center to the other with a different oxidation state through BL. The 1e-redox process involving a closed-shell precursor (M–BL–M) leads to an open-shell MV complex, which may be stabilized by charge delocalization over the [M–BL–M]$^{\bullet+/-}$ backbone. This redox interconversion between the neutral and MV states could be employed as a guiding principle for molecular switches. This is because the two electronic states are drastically different, and the charge-transfer phenomena can be finely controlled by the appropriate combination of the metal fragments and the bridging ligand, which should affect the conductance through the molecular junction based on the MV systems. Furthermore, few studies on the effect of the charge localization of MV complexes on the conductance of single molecules have been conducted.

Transition-metal acetylides exhibit significant application potential as components of molecular electronics because of their high conductance, attributed to the high-lying highest occupied molecular orbital (HOMO) energy levels due to the electron-rich metal fragments with *nd* electrons.[14–17] In addition, many of them are redox-active and can, therefore, be the switching triggers. Thus far, the redox-switching behavior of the organometallic mononuclear acetylide complexes in nanogaps has been investigated only for *in-situ* charging/discharging processes at low temperatures.[18–20] However, no example for operations at room temperature has been reported. This is mainly because of the intrinsic instability of the oxidized/reduced open-shell radical species of mononuclear organometallic complexes.[21,22] Herein, we report new redox-switchable dinuclear organometallic complexes based on electron-rich *trans*-Ru(dppe)$_2$ fragments, **1**^{R} (dppe: 1,2-bis(diphenylphosphino)ethane, Figure 1c). The following two advantages are noted for the (diethynylbenzene)diyl diruthenium complexes with the Ru–C≡C-*p*-C_6H_4–C≡C–Ru core skeletons: (1) the 1e-oxidized monocationic species can be stabilized by the diruthenium structures because of the formation of stable MV states, and (2) the electronic properties of the neutral and monocationic species can be finely modulated by the substituents on the central phenylene moiety.[23]

RESULTS AND DISCUSSION

Preparation and Characterization of the Monocationic Species ([1^{R}**][BARF]).** We synthesized the diruthenium acetylide complexes, **1**^{R} (R = OMe, H, or CF_3), and the details are described in Supporting Information (SI). To investigate the electrochemical properties of **1**^{R}, cyclic voltammetry was performed. All the three **1**^{R} complexes exhibited two reversible well-separated oxidation waves ranging from 0 to −500 mV (vs. the $FeCp_2/FeCp_2^+$ redox couple, Figure 2a). Based on the separation of the two redox waves (ΔE), the comproportionation constants (K_C) were determined to be 7.8 × 10^3 (**1**^{CF3}), 1.4 × 10^5 (**1**^{H}), and 1.8 × 10^6 (**1**^{OMe}). The large K_C values and the reversible redox waves indicated the formation of the monocationic species, [**1**^{R}]$^{+}$, which are thermodynamically stable in solutions.

Monocationic species, [**1**^{R}][BARF] (R = H and OMe; BARF^{-} = $B^{-}(3,5\text{-}(CF_3)_2C_6H_3)_4$), were synthesized by the treatment of **1**^{R} dissolved in CH_2Cl_2 with 1 equiv. of [$FeCp_2$][BARF], and were isolated in 64% ([**1**^{H}][BARF]) and 95% yields ([**1**^{OMe}][BARF]). Although our attempts to isolate [**1**^{CF3}][BARF] were unsuccessful probably because of its relatively small K_C value, the monocationic species, [**1**^{CF3}]$^{+}$, was stable in solution under ambient conditions (*vide supra*). Thus, in the following measurements, [**1**^{CF3}]$^{+}$ was generated *in situ* by the treatment of **1**^{CF3} with 1 equiv. of [$FeCp_2$][BARF].

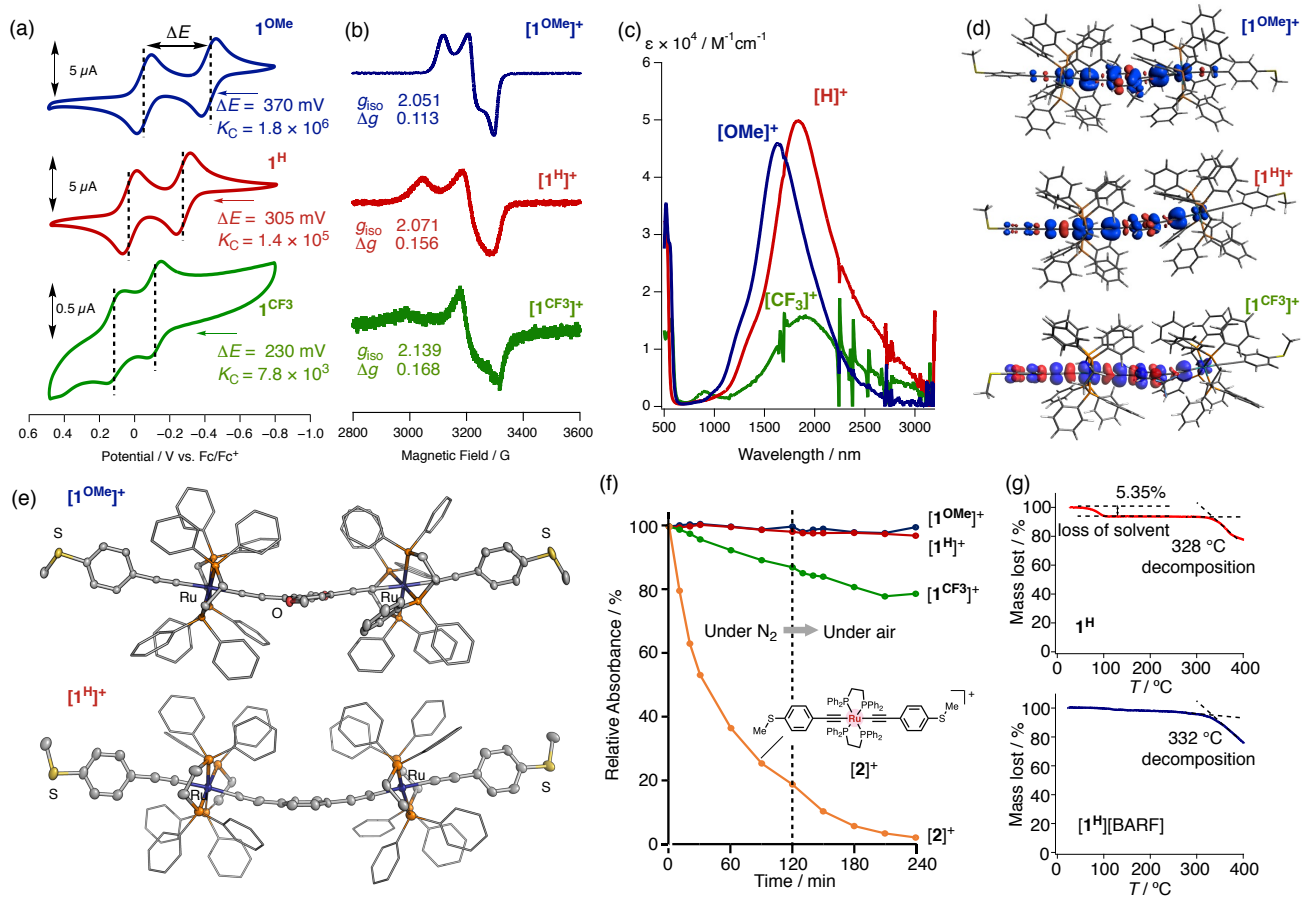

Figure 2. Physicochemical data for $\mathbf{1^R}$ and $[\mathbf{1^R}]^+$. (a) Cyclic voltammograms of $\mathbf{1^H}$ and $\mathbf{1^{OMe}}$: 1.0 mM in CH_2Cl_2; $\mathbf{1^{CF3}}$: 0.1 mM in CH_2Cl_2 (0.1 mM [*n*-Bu_4N][PF_6], W.E and C.E: Pt, R.E: Ag/Ag+, r.t.). (b) Electron spin resonance (ESR) spectra of $[\mathbf{1^R}]^+$ (113 K in CH_2Cl_2 glasses). (c) Visible–near infrared (Vis–NIR) spectra of $[\mathbf{1^R}]^+$ (0.1 mM in CH_2Cl_2). (d) Spin-density plots of $[\mathbf{1^R}]^+$ obtained by density functional theory (DFT) calculations [BLYP35-D3/Def2SVP, PCM(CH_2Cl_2)]. (e) X-ray structures of the cationic parts of $[\mathbf{1^{OMe}}]^+$ and $[\mathbf{1^H}]^+$. Hydrogen atoms and solvent molecules were omitted. Phenyl rings in the dppe ligands are depicted as wire models. (f) Time-course plots of the Vis–NIR absorptions of $[\mathbf{1^R}]$[BARF] (R = OMe, H, or CF_3) in CH_2Cl_2 ([complex] = 0.1 mM). The experiments were performed under a nitrogen atmosphere (from 0 to 120 min), after which the solutions were exposed to air. (g) Thermogravimetric (TG) thermograms of $\mathbf{1^H}$ and $[\mathbf{1^H}]$[BARF]. The amount of the CH_2Cl_2 solvent lost for $\mathbf{1^H}$ was in good agreement with the E.A. data.

The monocationic species, $[\mathbf{1^R}]$[BARF], were readily characterized by electron spin resonance (ESR) and near infrared (NIR) absorption spectroscopies (Figure 2b). The ESR spectra of $[\mathbf{1^R}]$[BARF] observed at 113 K in CH_2Cl_2 glasses revealed rhombic signals typical of the Ru(dppe)$_2$ complexes with an unpaired spin. The isotropic parameters ($g_{iso} = (g_1 + g_2 + g_3)/3$; $[\mathbf{1^{OMe}}]^+$ 2.051; $[\mathbf{1^H}]^+$ 2.071; $[\mathbf{1^{CF3}}]^+$ 2.139) are close to that for the free organic radical (g_{free} = 2.0023), and the split parameters (Δg) decrease with the electron-donating substituents ($[\mathbf{1^{OMe}}]^+$ 0.113; $[\mathbf{1^H}]^+$ 0.156; $[\mathbf{1^{CF3}}]^+$ 0.168). This suggests that the 1e-oxidized cation, $[\mathbf{1^{OMe}}]^+$, bears a large proportion of the organic parts. The intense NIR absorptions observed for $[\mathbf{1^R}]$[BARF] [λ_{max} = 1656 ($[\mathbf{1^{OMe}}]^+$), 1825 ($[\mathbf{1^H}]^+$), and 1903 nm ($[\mathbf{1^{CF3}}]^+$)] may stem from the intramolecular Ru–Ru interaction in $[\mathbf{1^R}]^+$ (Figure 2c). The absorptions disappear upon the addition of excess amounts of [$FeCp_2$][BARF] because of the formation of the corresponding dicationic species, $[\mathbf{1^R}]^{2+}$.

The spin-density distributions estimated by the DFT study revealed the even distribution on the two Ru atoms for $[\mathbf{1^{OMe}}]^+$ (0.15: 0.15) and the uneven distribution for $[\mathbf{1^H}]^+$ (0.47: 0.05) and $[\mathbf{1^{CF3}}]^+$ (0.42: 0.06, Figure 2d). Thus, complexes $[\mathbf{1^H}]^+$ and $[\mathbf{1^{CF3}}]^+$ are classified into charge-localized class II compounds, while the OMe derivative, $[\mathbf{1^{OMe}}]^+$, is a charge-delocalized class III compound.

The solid-state structures of $[\mathbf{1^H}]$[BARF] and $[\mathbf{1^{OMe}}]$[BARF] were characterized by X-ray diffraction analysis (Figure 2e). The diethynylbenzene moieties slightly distorted from the planarity ($\angle C_{Ar}$–C≡C = 168.5°). Compared with the neutral compound, $\mathbf{1^H}$ (Figure S8), the bonding features change from the acetylenic structure (Ru–C≡C–C_{Ar}) to the cumulenic structure (Ru=C=C=C_{Ar}), as indicated by the shortening of the Ru–C (2.033 Å) and ≡C–C_{Ar} bonds (1.425 Å), as well as the lengthening of the C≡C bonds ($d_{C\equiv Cav}$ = 1.217 Å) [cf. $\mathbf{1^H}$: $d_{Ru\text{-}Cav}$ (2.050 Å), $d_{\equiv C\text{-}CArav}$ (1.446 Å), and $d_{C\equiv Cav}$ (1.223 Å)]. In accordance with the Robin–Day classification discussed above, the unsymmetrical bonding feature of the Ru–C≡C–Ar–C≡C–Ru moiety in $[\mathbf{1^H}]^+$ is in contrast to the virtually symmetrical feature in $[\mathbf{1^{OMe}}]^+$ (Tables S2, 3). These features are also supported by the DFT study.

Stability and Reversibility of the Switching Behavior. The high thermal stability of [**1**^{R}]$^{+}$ under ambient conditions is highlighted by the time-course analysis of the Vis–NIR absorptions of [**1**^{R}][BARF] dissolved in CH_2Cl_2. The dinuclear complexes, [**1**^{R}][BARF], were stable for 2 h (enough for the scanning tunneling microscope-break-junction (STM-BJ) measurements, see below) both under a nitrogen atmosphere and in air, as evidenced by the retention of the Vis–NIR absorptions ([**1**^{OMe}]$^{+}$: 100%; [**1**^{H}]$^{+}$: 98%; [**1**^{CF3}]$^{+}$: 79%), whereas the mononuclear analog, [**2**]$^{+}$, rapidly and almost completely decomposed under the same conditions (Figure 2f). These results proved that exploiting the dinuclear skeleton is one of the effective strategies for stabilizing the monocationic radical species containing the $Ru(dppe)_2$ fragments. In addition, because the sequential treatment of **1**^{H} with [$FeCp_2$][BARF] and $FeCp^*_2$ caused reversible Vis–NIR spectral changes (Figure S12), the redox process can be repeated at least six times in solution.

Furthermore, the thermogravimetric analysis of the neutral **1**^{H} and cationic [**1**^{H}][BARF] complexes revealed that they were stable up to around 300°C (Figure 2g). This high thermal stability in the solid state will benefit the device fabrication and switching operation in the nanogap.

STM-BJ Study. Using the STM-BJ technique,[24] we measured the single-molecule conductances of **1**^{R} and [**1**^{R}][BARF] in mesitylene (Figures 3a–c). The 1D histograms of both the neutral and monocationic species revealed the conductance features in the range of 10^{-2}–10^{-6} G_0. The statistical analyses afforded the single-molecule conductances of the neutral and monocationic species, which are summarized in Table 1, and the conductance plot against the Hammett parameter (σ[25]) is shown in Figure 3d. The features of the 2D histograms extended over 2.5 nm are consistent with the connection of [**1**^{R}]$^{n+}$ at the sulfur atoms in the terminal thiomethyl anchor groups ($d_{S\cdots S}$ ~3.0 nm) when the snapback distance (~0.5 nm) is considered (Figures 5e, f, and S17a). The conductance of the neutral species, **1**^{R}**,** increases upon the introduction of the electron-donating substituents (225-fold from **1**^{CF3} to **1**^{OMe}). Compared with the case in the molecular junctions composed of simple organic molecules, such as phenylenediamine[26] and carbazole derivatives,[27] the conductance change in **1**^{R} induced by the substituents is remarkable. Conversely, the conductance of the monocationic species [**1**^{R}]$^{+}$ follows the opposite trend, i.e., the conductance decreases from [**1**^{CF3}]$^{+}$ to [**1**^{OMe}]$^{+}$ by 0.4-fold. Consequently, the ON/OFF switching ratio, which is the ratio of the conductances of the monocationic species ([**1**^{R}]$^{+}$) relative to those of the neutral ones (**1**^{R}), drastically changes from 191 (for [**1**^{CF3}]$^{+}$/**1**^{CF3}) to 48 (for [**1**^{H}]$^{+}$/**1**^{H}) and then to 0.4 (for [**1**^{OMe}]$^{+}$/**1**^{OMe}). These results show that the organometallic molecular switches (**1**^{R}–[**1**^{R}]$^{+}$) can be facilely and effectively modulated by the substituents (R) on the central aromatic rings.

Furthermore, we carried out *in-situ* switching experiments (Figure 3g). The addition of an equimolar amount of [$FeCp_2$][BARF] to a mesitylene solution of **1**^{H} caused a shift in the conductance peak to 10^{-3} G_0, indicating the generation of [**1**^{H}]$^{+}$. Inversely, the *in-situ* reduction of the mesitylene solution of [**1**^{H}][BARF] by $FeCp^*_2$ (Cp*; 1,2,3,4,5-pentamethylcyclopentadienyl) led to the replacement of the conductance peak of [**1**^{H}][BARF] with a new peak around 10^{-5} G_0, which was superimposable on that of **1**^{H}. Thus, the switching behavior could be reproduced reversibly in solution.

DFT–NEGF study. To gain insights into the tunable ON/OFF ratios, we carried out DFT–NEGF calculations on the molecular junction models of [**1**$^{R'}$]$^{n+}$ (n = 0, 1) with truncated bis(dimethylphosphino)methane ligands, with the pyramidal Au clusters attached to the terminal sulfur atoms (Figures 3h, i).[28–30] The HOMO transmission peaks of the neutral species are located close to the Fermi energy level (E_F) of the electrode (Au) and are sensitive to the substituents. The HOMO transmission peaks approach E_F as the electron-donating character of the substituents increases (CF_3 (−0.23 eV) → H (−0.10 eV) → OMe (−0.03 eV); highlighted as the square marks in Figure 3h), which is also supported by the HOMO energies estimated from the cyclic voltammograms [CF_3 (−4.93 eV) → H (−4.76 eV) → OMe (−4.61 eV)). The theoretically estimated conductance of **1**$^{OMe'}$ significantly increases compared with those of **1**$^{H'}$ and **1**$^{CF3'}$ because the HOMO transmission peak of **1**$^{OMe'}$ is considerably close to the Fermi level. Since the slope of the transmission spectra at E_F is steep, small shifts in the transmission peak energy lead to significant conductance changes. In contrast, the HOMO–LUMO (lowest unoccupied molecular orbital) gaps of simple organic molecules are, in general, overly large that the conduction peaks are located far from the Fermi level. Resultantly, the conductance around E_F decreases to flatten the transmission curve around E_F, leading to the insensitivity of the conductance to the substituents.

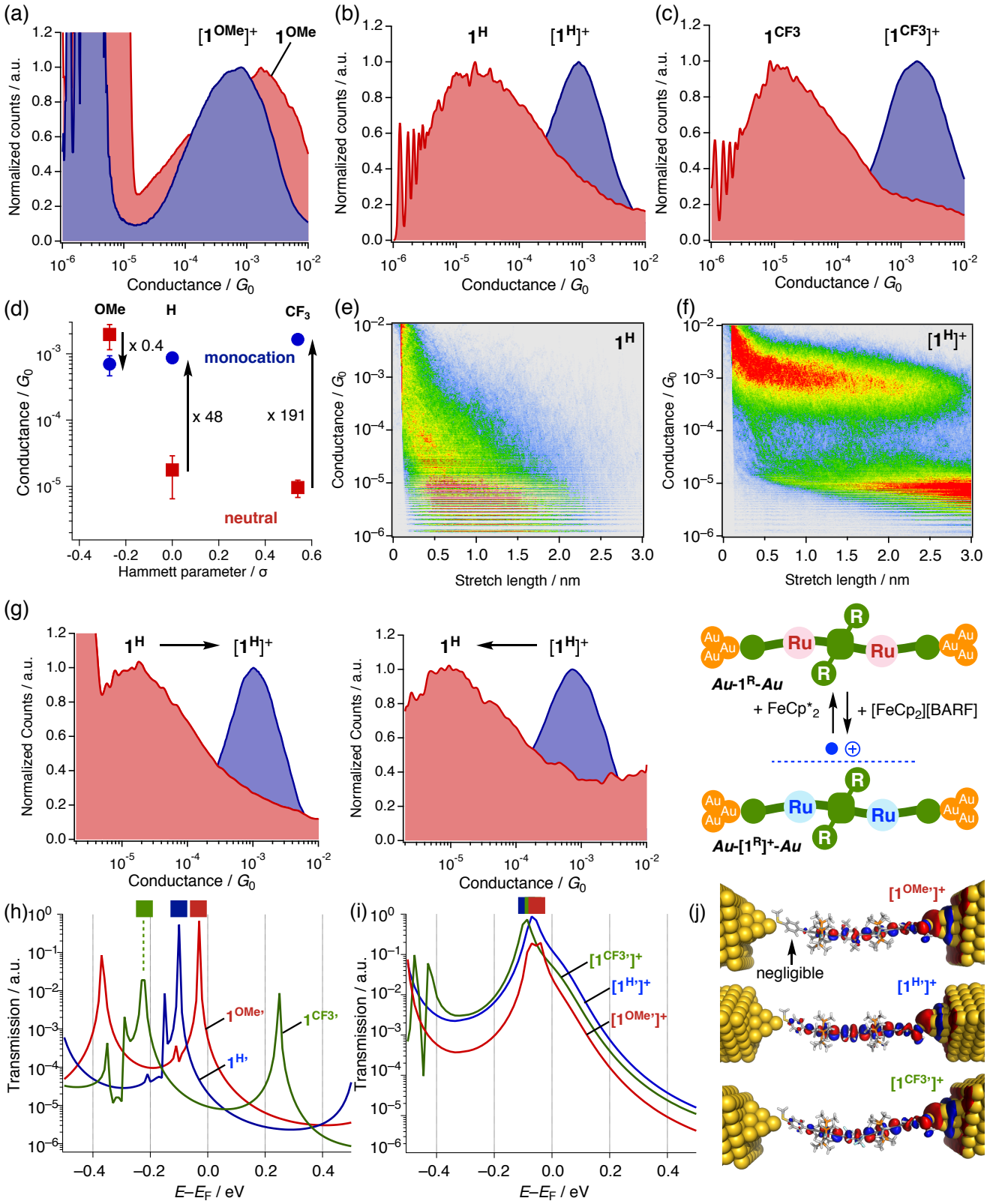

Figure 3. One-dimensional histograms obtained by the STM-BJ study of (a) $[\mathbf{1}^{\mathbf{OMe}}]^{n+}$, (b) $[\mathbf{1}^{\mathbf{H}}]^{n+}$, and (c) $[\mathbf{1}^{\mathbf{CF3}}]^{n+}$ (n = 0,1). (d) Plots of the conductance versus the Hammett parameters. (e, f) Two-dimensional histograms of $\mathbf{1}^{\mathbf{H}}$ and $[\mathbf{1}^{\mathbf{H}}]$[BARF]. (g) Sequential *in-situ* oxidation of $\mathbf{1}^{\mathbf{H}}$ with [FeCp$_2$][BARF] and reduction of $[\mathbf{1}^{\mathbf{H}}]$[BARF] with FeCp*$_2$. Transmission spectra for (h) the ***Au***-$\mathbf{1}^{\mathbf{R'}}$-***Au*** and (i) ***Au***-$[\mathbf{1}^{\mathbf{R'}}]^{+}$-***Au*** junctions (***Au***; Au cluster). Square marks indicate the dominant transmission peaks. (j) Dominant transmission eigenchannels at the Fermi level for the ***Au***–$[\mathbf{1}^{\mathbf{R'}}]^{+}$–***Au*** junctions.

Table 1. Experimental and theoretical conductances of $\mathbf{1^R}$ and $[\mathbf{1^R}]^+$.

	Experiment			DFT–NEGF	
	Conductance/× 10^{-5} G_0		ON/OFF ratio	Conductance/× 10^{-5} G_0	
R in $\mathbf{1^R}$ and $[\mathbf{1^R}]^+$	Neutral ($\mathbf{1^R}$)	Monocation ($[\mathbf{1^R}][\mathrm{BARF}]$)		Neutral ($\mathbf{1^{R'}}$)	Monocation ($[\mathbf{1^{R'}}]^+$)
OMe	200 (± 80)	71 (± 44)	0.35	57	2050
H	1.8 (± 1.1)	87 (± 11)	48	2.2	10700
CF_3	0.89 (± 0.28)	170 (± 20)	191	0.96	4500

Contrarily, the energy levels of the transmission peaks of the monocationic species, $[\mathbf{1^{R'}}]^+$, are in a very narrow range irrespective of the R (Figure 3i). This phenomenon can be interpreted in terms of the pinning effect, i.e., the singly occupied orbital of open-shell species is placed at the energy level close to the Fermi energy. Consequently, the molecular junctions exhibit almost identical conductance values regardless of the molecular backbone.[31] However, the BJ study of the monocationic species revealed a slight decrease in the conductance upon the introduction of the OMe substituents (0.4-fold; $[\mathbf{1^{CF3}}]^+/[\mathbf{1^{OMe}}]^+$). The trend is also confirmed by the calculations; the conductance peak of $[\mathbf{1^{OMe'}}]^+$ is weaker than those of $[\mathbf{1^{H'}}]^+$ and $[\mathbf{1^{CF3'}}]^+$. According to the transmission eigenchannels (Figure 3j), the contribution of one of the two terminal anchor groups of $[\mathbf{1^{OMe'}}]^+$ (indicated with the arrow) is lower than those of $[\mathbf{1^{H'}}]^+$ and $[\mathbf{1^{CF3'}}]^+$, indicating the weak electronic coupling between the molecule and the electrode.

The observed result that the MV complexes show similar conductances regardless of the charge-delocalized states contradicts our expectation based on the Marcus–Hush regime.[32–34] Highly charge-delocalized class III systems are expected to exhibit a high carrier mobility, while class II systems should show a low carrier mobility in solution and the bulk solid state. However, our results suggest that, for the single-molecule conductance, there is no apparent relationship between the charge delocalization and conductance, and even the trend is inversed, i.e., the conductances of the class II systems ($[\mathbf{1^H}]^+$ and $[\mathbf{1^{CF3}}]^+$) are higher that those of the class III system ($[\mathbf{1^{OMe}}]^+$). This discrepancy can be interpreted as follows: in the coherent tunneling process, the interaction between the metal electrodes and the molecule dominates the conductance (pinning effect) rather than the intramolecular interaction. By contrast, the Marcus–Hush-type charge-transfer phenomena deal with the thermal-activation processes accompanying the solvent reorganization. Thus, the significant MV character in the molecular junction may appear when the conductance mechanism is dominated by the thermally activated hopping process.[35]

Switching Behavior in the Nanogap. The switching function of the $\mathbf{1^R}$–$[\mathbf{1^R}]^+$ system was further studied by the nanogap technique. The conductance obtained by the STM-BJ technique is not for a specific molecule because after the BJ step, another molecule is introduced into the electrodes, and the process is repeated many times. Thus, we can obtain the averaged features of the molecules in the sample solution. Contrary to the dynamic STM-BJ technique, the static nanogap technique described below does not involve BJ steps, and the molecules sandwiched between the nanogap stay there during the measurement so that the changes in the particular molecules fixed between the electrodes can be observed. Therefore, we can observe the switching process of the fixed molecules induced by *in-situ* redox processes.

A 1 nm-sized nanogap (**NG0**) was prepared following a previously reported procedure.[36] The I–V characteristic of the **NG**s obtained by the immersion of the **NG0** in CH_2Cl_2 solutions of $\mathbf{1^H}$ ($\mathbf{NG1^H}$) or $[\mathbf{1^H}][PF_6]$ ($\mathbf{NG}[\mathbf{1^H}]^+$), followed by drying under a nitrogen stream, revealed the resistances of 7.96 GΩ ($\mathbf{NG1^H}$) and 1.61 GΩ ($\mathbf{NG}[\mathbf{1^H}]^+$) at 0.1 V, which were significantly smaller than the value obtained with a bare **NG0** (546 GΩ) (Figures 4a, b).[37] Furthermore, we performed surface-enhanced Raman scattering (SERS) experiments on $\mathbf{NG1^H}$ to confirm the molecular finger print in the nanogap.[38–41] The Raman spectrum obtained from $\mathbf{NG1^H}$ showed characteristic signals at 520, 1000, 1070, and 1175 cm^{-1}, corresponding to those observed for the bulk sample of $\mathbf{1^H}$, as compared in Figure 4c. The Raman-mapping images provided high Raman intensity points for the nanogap (Figure 4c, inset), supporting the molecular junction formation.

In-situ ON/OFF experiments were performed for the nanogap containing $\mathbf{1^H}$ described above ($\mathbf{NG1^H}$) (Figure 4d). The immersion of $\mathbf{NG1^H}$ in a CH_2Cl_2 solution of $[FeCp_2][\mathrm{BARF}]$ induced an increase in the conductance by a factor of 42 (at 1 V), which corresponds to the formation of the nanogap with the $[\mathbf{1^H}]^+$ bridges. The conductance was recovered by further treatment of $\mathbf{NG}[\mathbf{1^H}]^+$ with a mesitylene solution of $FeCp^*_2$. Thus, this study demonstrated the ON/OFF switching behavior of the dinuclear molecular systems, $\mathbf{1^R}$–$[\mathbf{1^R}]^+$, and their potential for application in molecular devices.

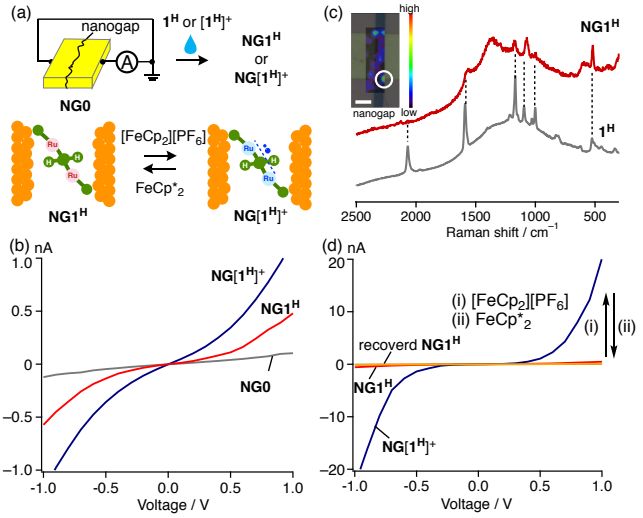

Figure 4. (a) Schematic images of the preparation of the nanogap junctions (**NG1^{H}** and **NG[1^{H}]**$^{+}$), and the *in-situ* oxidation and reduction of **NG1^{H}** and **NG[1^{H}]**$^{+}$. (b) I–V curves of **NG0, NG1^{H}**, and **NG[1^{H}]**$^{+}$. (c) SERS spectra of **NG1^{H}** and the bulk samples of **1^{H}**. The inset shows a Raman-mapping image of **NG1^{H}**. A high Raman intensity point (highlighted by a circle) was observed for the nanogap.[42] The white scale bar indicates 10 μm. (d) *In-situ* ON/OFF switching experiments on **NG1^{H}** with the sequential addition of $[FeCp_2][PF_6]$ and $FeCp^*_2$.

CONCLUSION

In summary, we developed new organometallic molecular switches, **1^{R}**–**[1^{R}]**$^{+}$, that respond to redox stimuli. Both the neutral and monocationic MV complexes were stable under ambient conditions (at room temperature in air). Notably, the monocationic species, otherwise usually unstable (particularly mononuclear systems), were stabilized by the *d*π–*p*π systems delocalized widely over the Ru–C≡C–Ar–C≡C–Ru linkages, affording stable MV states. The single-molecule conductance study highlighted the switching behavior of the molecules. Interestingly, the ON/OFF switching ratio could be facilely controlled by the substituents embedded in the bridging linkers up to a factor of *ca.* 200. This was mainly due to the drastic change in the conductance of the neutral species. This change is responsible for the high-lying HOMO orbitals, attributed to the electron-rich ruthenium fragments. Additionally, we demonstrated the switching behavior in the nanogap, which is beneficial for the fabrication of molecular devices. Notably, this paper presents a rare example of a single-molecule conductance study of MV complexes[43,44] and the achievement of a tunable ON/OFF ratio. Thus, we have revealed that dinuclear organometallic systems offer a new platform for modulable molecular switches, which will promote the development of new molecular electronics.

AUTHOR INFORMATION

Corresponding Authors

Yuya Tanaka–
orcid.org/0000-0002-0674-660X; Email:
ytanaka@res.titech.ac.jp
Munetaka Akita–
orcid.org/0000-0001-7007-9621; Email: akitatit@icloud.com

Author Contributions

YT and MA conceived the project. NM carried out all the experiments and NM and YT analyzed data. YT, TO, and HT contributed the theoretical study. SK measured SERS spectra. NM and YN performed nanogap experiments. SF and TN supervised STM-BJ experiments. The manuscript was drafted by YT and edited by MA. All authors read and approved the final manuscript.

Author Information Notes

† These authors contributed equally to this work.

Notes

The authors declare no competing financial interest.

ACKNOWLEDGMENT

We gratefully thank Prof. Hideyuki Otsuka and Mr. Takumi Yamamoto (Tokyo Tech) for their kind help with EPR measurements. This work was supported by JSPS KAKENHI Grant Numbers 18K05139 and 21K05211 (YT), and JST, PRESTO Grant Number JPMJPR2115 (TO). YT acknowledges research grants from ENEOS Tonengeneral Research/Development Encouragement & Scholarship Foundation, The Asahi Glass Foundation, Inamori Foundation, Tokyo Kasei Chemical Promotion foundation and Tokuyama Science Foundation. The theoretical calculations were performed by using computers in the Research Center for Computational Science, Okazaki, Japan.

REFERENCES

1. Kiguchi, M. *et al.* Single Molecular Resistive Switch Obtained via Sliding Multiple Anchoring Points and Varying Effective Wire Length. *J. Am. Chem. Soc.* **136**, 7327–7332 (2014).
2. Pei, L. Q. *et al.* Mechanically Induced Switching between Two Discrete Conductance States: A Potential Single-Molecule Variable Resistor. *ACS Appl. Mater. Interfaces* **13**, 57646–57653 (2021).
3. Li, J. *et al.* Mechanical Single-Molecule Potentiometers with Large Switching Factors from Ortho-Pentaphenylene Foldamers. *Nat. Commun.* **12**, 167 (2021).
4. Li, Z. *et al.* Single-Molecule Sensing of Environmental pH—An STM Break Junction and NEGF-DFT Approach. *Angew. Chem. Int. Ed.* **53**, 1098–1102 (2014).
5. Yoshihara, Y., Fujii, S., Higashibayashi, S., Kiguchi, M. & Nishino, T. Single-Molecule Electric Switching Induced by Acid–Base Reaction. *Chem. Lett.* **50**, 1271–1273 (2021).
6. Dulić, D. *et al.* One-Way Optoelectronic Switching of Photochromic Molecules on Gold. *Phys. Rev. Lett.* **91**, 207402 (2003).
7. Whalley, A. C., Steigerwald, M. L., Guo, X. & Nuckolls, C. Reversible Switching in Molecular Electronic Devices. *J. Am. Chem. Soc.* **129**, 12590–12591 (2007).
8. Jia, C. *et al.* Covalently Bonded Single-Molecule Junctions with Stable and Reversible Photoswitched Conductivity. *Science* **352**, 1443–1445 (2016).
9. Li, Y. *et al.* Three-State Single-Molecule Naphthalenediimide Switch: Integration of a Pendant Redox Unit for Conductance Tuning. *Angew. Chem. Int. Ed.* **54**, 13586–13589 (2015).
10. Yin, X. *et al.* A Reversible Single-Molecule Switch Based on Activated Antiaromaticity. *Sci. Adv.* **3**, eaao2615 (2017).
11. Chen, Y. *et al.* Towards Responsive Single-Molecule Device. *Chin. J. Chem.* **39**, 421–439 (2021).
12. Li, Z. *et al.* Regulating a Benzodifuran Single Molecule Redox Switch via Electrochemical Gating and Optimization of Mole-

cule/Electrode Coupling. *J. Am. Chem. Soc.* **136**, 8867–8870 (2014).
13. Creutz, C. & Taube, H. Direct Approach to Measuring the Franck-Condon Barrier to Electron Transfer between Metal Ions. *J. Am. Chem. Soc.* **91**, 3988–3989 (1969).
14. Ren, T. Diruthenium σ-Alkynyl Compounds: A New Class of Conjugated Organometallics. *Organometallics* **24**, 4854–4870 (2005).
15. Lissel, F. *et al*. Organometallic Single-Molecule Electronics: Tuning Electron Transport through X(Diphosphine)2FeC4Fe(diphosphine)2X Building Blocks by Varying the Fe–X–Au Anchoring Scheme from Coordinative to Covalent. *J. Am. Chem. Soc.* **136**, 14560–14569 (2014).
16. Tanaka, Y., Kiguchi, M. & Akita, M. Inorganic and Organometallic Molecular Wires for Single-Molecule Devices. *Chem. Eur. J.* **23**, 4741–4749 (2017).
17. Milan, D. C., Vezzoli, A., Planje, I. J. & Low, P. J. Metal Bis(Acetylide) Complex Molecular Wires: Concepts and Design Strategies. *Dalton Trans.* **47**, 14125–14138 (2018).
18. Schwarz, F. *et al*. Field-Induced Conductance Switching by Charge-State Alternation in Organometallic Single-Molecule Junctions. *Nat. Nanotechnol.* **11**, 170–176 (2016).
19. For a molecular wire with a combination of redox and photoirradiation, see Ref. 20.
20. Meng, F. *et al*. Orthogonally Modulated Molecular Transport Junctions for Resettable Electronic Logic Gates. *Nat. Commun.* **5**, 3023 (2014).
21. Schauer, P. A. & Low, P. J. Ligand Redox Non-Innocence in Transition-Metal σ-Alkynyl and Related Complexes. *Eur. J. Inorg. Chem.* **2012**, 390–411 (2012).
22. Tanaka, Y. & Akita, M. Organometallic Radicals of Iron and Ruthenium: Similarities and Dissimilarities of Radical Reactivity and Charge Delocalization. *Coord. Chem. Rev.* **388**, 334–342 (2019).
23. Fox, M. A. *et al*. Simultaneous Bridge-Localized and Mixed-Valence Character in Diruthenium Radical Cations Featuring Diethynylaromatic Bridging Ligands. *J. Am. Chem. Soc.* **133**, 18433–18446 (2011).
24. Xu, B. & Tao, N. J. Measurement of Single-Molecule Resistance by Repeated Formation of Molecular Junctions. *Science* **301**, 1221–1223 (2003).
25. Hansch, C., Leo, A. & Taft, R. W. A Survey of Hammett Substituent Constants and Resonance and Field Parameters. *Chem. Rev.* **91**, 165–195 (1991).
26. Venkataraman, L. *et al*. Electronics and Chemistry: Varying Single-Molecule Junction Conductance Using Chemical Substituents. *Nano Lett.* **7**, 502–506 (2007).
27. Yzambart, G. *et al*. Thermoelectric Properties of 2,7-Dipyridylfluorene Derivatives in Single-Molecule Junctions. *J. Phys. Chem. C Nanomater. Interfaces* **122**, 27198–27204 (2018).
28. Brandbyge, M., Mozos, J.-L., Ordejón, P., Taylor, J. & Stokbro, K. Density-Functional Method for Nonequilibrium Electron Transport. *Phys. Rev. B* **65**, 165401 (2002).
29. Tada, T., Kondo, M. & Yoshizawa, K. Green's Function Formalism Coupled with Gaussian Broadening of Discrete States for Quantum Transport: Application to Atomic and Molecular Wires. *J. Chem. Phys.* **121**, 8050–8057 (2004).
30. For detailed structures of molecular junction model, see SI.
31. Wang, K. *et al*. Charge Transfer Complexation Boosts Molecular Conductance through Fermi Level Pinning. *Chem. Sci.* **10**, 2396–2403 (2019).
32. Thomas, G. A. *et al*. Electrical Conductivity of tetrathiafulvalenium-tetracyanoquinodimethanide (TTF-TCNQ). *Phys. Rev. B* **13**, 5105–5110 (1976).
33. Demadis, K. D., Hartshorn, C. M. & Meyer, T. J. The Localized-to-Delocalized Transition in Mixed-Valence Chemistry. *Chem. Rev.* **101**, 2655–2686 (2001).
34. Xie, L. S. *et al*. Tunable Mixed-Valence Doping Toward Record Electrical Conductivity in a Three-Dimensional Metal–Organic Framework. *J. Am. Chem. Soc.* **140**, 7411–7414 (2018).
35. Ie, Y. *et al.* Improving Intramolecular Hopping Charge Transport via Periodical Segmentation of π-Conjugation in a Molecule. *J. Am. Chem. Soc.* **143**, 599–603 (2021).
36. Naitoh, Y. *et al*. Self-Aligned Formation of Sub 1 nm Gaps Utilizing Electromigration during Metal Deposition. *ACS Appl. Mater. Interfaces* **5**, 12869–12875 (2013).
37. Probably due to the large size of BARF salt, no resistance change was observed before and after immersion in [**1**$^{\mathbf{H}}$][BARF]. Therefore we choose small PF_6^-salt.
38. Nie, S. & Emory, S. R. Probing Single Molecules and Single Nanoparticles by Surface-Enhanced Raman Scattering. *Science* 275, 1102–1106, doi:10.1126/science.275.5303.1102 (1997).
39. Suzuki, S. *et al*. Effect of the Molecule–Metal Interface on the Surface-Enhanced Raman Scattering of 1,4-Benzenedithiol. *J. Phys. Chem. C* **120**, 1038–1042 (2016).
40. Langer, J. *et al*. Present and Future of Surface-Enhanced Raman Scattering. *ACS Nano* **14**, 28–117 (2020).
41. SERS measurements were carried out with a commercial laser Raman spectrometer (NRS 4500, JASCO Corporation, Japan). The wavelength and power of the excitation laser were 785 nm and 3 mW, respectively.
42. The normal Raman spectrum of the **1**$^{\mathbf{H}}$ was obtained with the laser irradiation for 20 s. The intensity of the vibrational mode observed at 1175 cm^{-1} was mapped with the resolution of 3 μm. The mapping area was 12 μm x 42 μm.
43. Liu, I. P.-C. *et al.* A New Generation of Metal String Complexes: Structure, Magnetism, Spectroscopy, Theoretical Analysis, and Single Molecular Conductance of an Unusual Mixed-Valence Linear [Ni5]8+ Complex. *Chem. Eur. J.* **13**, 8667–8677 (2007).
44. Ting, T.-C. *et al*. Energy-Level Alignment for Single-Molecule Conductance of Extended Metal-Atom Chains. *Angew. Chem. Int. Ed.* **127**, 15960–15964 (2015).